IEEE Access
Multidisciplinary | Rapid Review | Open Access Journal

Received 23 July 2024, accepted 22 August 2024, date of publication 30 August 2024, date of current version 10 September 2024.

Digital Object Identifier 10.1109/ACCESS.2024.3452125

RESEARCH ARTICLE

Designs of Dual-Band Circularly-Polarized Filtering Antennas Using Multiple Resonant Modes

CHENG-FANG CAO[1], ERIC S. LI[1], HUAYAN JIN[2], (Member, IEEE), DONGXU CHEN[3], AND KUO-SHENG CHIN[4], (Senior Member, IEEE)

[1]Department of Electronic Engineering, National Taipei University of Technology, Taipei 10608, Taiwan
[2]Key Laboratory of RF Circuits and System of Ministry of Education, Hangzhou Dianzi University, Hangzhou 310018, China
[3]College of Computer and Information, Hohai University, Nanjing, Jiangsu 210098, China
[4]Department of Electronics Engineering, Chang Gung University, Taoyuan 333, Taiwan

Corresponding author: Kuo-Sheng Chin (kschin@mail.cgu.edu.tw)

This work was supported by the National Science and Technology Council, Taiwan, under Grant NSTC 112-2221-E-182-035 and Grant NSTC 112-2221-E-182-036.

ABSTRACT This work developed two cavity-backed slot antennas based on substrate integrated waveguide (SIW) technology. The designs offer the advantages of single-layer structure, dual-band operations, circular polarization, and filtering performance. Antenna I features a perturbed aperture on an SIW cavity and four cross slots distributed near its corners to excite seven resonant modes. Among them, two sets of orthogonal modes, namely TE_{120}/TE_{210} and TE_{230}/TE_{320}, are used to create the first (3.7 GHz) and the second (5.6 GHz) operating bands, respectively, and to establish dual-band circularly-polarized properties for 5G NR n46 and n78 applications. The remaining three modes, TE_{110}, TE_{220}, and TE_{330}, serve to generate radiation nulls to increase stopband rejection. Measured results indicated a peak gain value up to 7.1 dBic. The rejection levels at the lower, middle, and upper stopbands were 23, 10, and 17 dB, respectively. Antenna II further improves the rejection level at the middle stopband by introducing three complementary split-ring resonators (CSRRs) to the SIW feed line. It allows a broader stopband between the two passbands and enhances the corresponding rejection level. The middle CSRR is etched on the top of the SIW, whereas the other two CSRRs are on the bottom to avoid undesired resonance and to improve the rejection level effectively. The measured realized gain was as high as 7.78 dBic with excellent filtering characteristics. The rejection levels of 24, 24, and 20 dB were observed at the lower, middle, and upper stopbands, respectively.

INDEX TERMS Circularly polarized, complementary split-ring resonator (CSRR), dual-band antenna, filtering antenna, multiple resonant modes, substrate integrated waveguide cavity (SIWC).

I. INTRODUCTION

Antennas and filters are crucial components of wireless communication systems. Typically, their designs are independent of each other, and the connections between them would require additional circuitries, which lead to increases in sizes and insertion loss. Filtering antennas integrate the two functionalities into a single design to solve the above problems [1], [2], and provide excellent selectivity for gain response. Radiation nulls were introduced in structures to improve filtering response and reduce size and insertion loss in early studies [3], [4], [5], [6], [7], [8], [9], [10], [13], [14], [16], [17], [20], [21]. In [3], stubs were employed to generate radiation nulls in antenna gain performance to achieve a band-pass response. In [4], parasitic lines and loops were placed next to a rectangular loop antenna with openings created at its two lateral sides. The rectangular loop antenna exhibits great selectivity at the lower frequency end, while the parasitic lines and loops improve selectivity at the higher end. Creating slots at a radiating antenna and a ground plane was proposed

The associate editor coordinating the review of this manuscript and approving it for publication was Weiren Zhu.

in [5]. Filtering response was accomplished via the band-stop property of the slot resonance. A structure featuring stacked patches was reported in [6]. The main patch loaded with grounded metallic vias allowed the antenna to resonate in a higher-order mode to create radiation nulls. An H-shaped feed network was proposed in [7] to establish high-pass filtering response for better frequency selectivity. In [8], patches were distributed at specific locations of 0.5λ, 1λ, and 2λ along a feed network to generate opposite currents on the patches to create radiation nulls. Reference [9] shows a cross-shaped patch with a differential feed network and a structure of four stacked parasitic patches to produce radiation nulls.

The technique of substrate integrated waveguide (SIW) offers the advantages of low loss, high quality factor, and a planar structure. An SIW antenna comprising a slot and two U-shaped cracks was presented in [10]. One of the U-shaped slots introduced radiation nulls, while the other slot increased its bandwidth. Reference [12] presents an SIW cavity-backed slot antenna design. A slot created on a rectangular cavity radiated in TE_{120} mode with a bandwidth of 1.7%. This antenna only required a single-layer substrate, offering a simple structure and ease in fabrication. In [13], the fundamental mode of an SIW cavity was excited and electromagnetic mixed coupling was generated to create two radiation nulls for quasi-elliptic filtering response. A hybrid antenna design integrating an SIW cavity-backed slot and a patch is disclosed in [14]. A bandwidth of 9.14% was achieved through the simultaneous excitation of a TE_{210} mode from the SIW cavity and a TM_{11} mode from the patch. Since a TE_{110} mode could be excited to exhibit an odd-symmetrical distribution of current directions, radiation nulls could be obtained. In addition, the electromagnetic mixed coupling between the SIW cavity and the patch could produce another radiation null to improve selectivity.

Circular polarization offers the advantages of reduction in polarization mismatch as well as multi-path interference. Therefore, the development of circularly-polarized (CP) filtering antennas is crucial for wireless communications [15−17]. In [15], a third-order Chebyshev filtering response was achieved using two cavity resonators and a CP patch antenna. A CP filtering antenna design presented in [16] integrated a cavity-backed slot and a patch to achieve a 12% operating bandwidth. Reference [17] discloses a broadband CP filtering antenna array design. The circular polarization was realized via small perturbations to excite TE_{120}/TE_{210} modes. Furthermore, the excitation of TE_{110} and TE_{220} modes generated radiation nulls at lower and higher frequency ends, respectively. As the wireless communication systems move towards dual-band operations, antenna designs need to incorporate dual-band functionality accordingly [18], [19]. The radiators shown in [18] consisted of C-shaped and L-shaped lines. The C-shaped lines generated circular polarization at higher frequencies, as opposed to the L-shaped lines operating at lower frequencies to accomplish dual-band CP operations. Reference [19] shows two radiating slots bent at a quarter length from the short-circuited end. 0.5λ and 1λ modes were utilized to develop a dual-band CP antenna. However, these antenna designs from the two references above didn't offer the filtering functionality. Reference [20] proposed a dual-band CP filtering antenna whose low-frequency and high-frequency resonances were realized by four short-end arcs and four open-end branches, respectively. Dual-band coupled stripline filters were cascaded to the radiator for filtering response and bandwidth enhancement. Currently, antenna designs capable of dual-band operations, circular polarization, and filtering functionality are rare, and therefore present a challenge to the antenna community.

This work develops two cavity-backed slot antennas (Antenna I and II) based on SIW technology, which have the advantages of single-layer structure, dual-band, circular polarization, and filtering performance. The rest of this paper is organized as follows: In Section II, Antenna I etched a perturbed aperture and cross-shaped slots on the top surface of the SIW cavity, and added patch and notch perturbation structures. A total of seven resonant modes are excited to achieve dual-band circular polarization and create radiation nulls. Second III proposes an improved design of Antenna II. By introducing three CSRRs to the SIW feed line, the rejection level can be improved significantly. At last, the paper is concluded in Section IV.

II. DUAL-BAND CIRCULARLY-POLARIZED FILTERING ANTENNA (ANTENNA I)

The proposed dual-band CP filtering antenna features a square SIW cavity (called SIWC) with multiple resonant modes and is designed to operate at 3.7 GHz/5.6 GHz for applications in 5G NR n46 and n78 bands. Fig. 1(a) shows the single-layer SIWC configuration. The substrate for this design is Rogers RT/Duroid 5880 ($\varepsilon_r = 2.2$, $\tan\delta = 0.0009$). The initial length of the SIWC can be calculated using

$$f_{mn0} = c_v\sqrt{(m/L)^2 + (n/W)^2}/2\sqrt{\varepsilon_r} \tag{1}$$

where c_v is the speed of light, and m and n are the numbers of periodic half-waves in the x- and y-directions, respectively.

A. RESONANT MODE ANALYSIS OF SIWC

The full-wave EM software ANSYS HFSS was employed to conduct simulations. Since multiple resonant modes are used to synthesize the dual-band CP filtering response, Fig. 2(a) shows the resonant frequency versus mode number of the proposed SIWC using the eigenmode method. Fig. 2(b) illustrates the electric field distributions of the first eight resonant modes, Mode1−Mode8, which are TE_{110}, TE_{120}, TE_{210}, TE_{220}, TE_{130}, TE_{310}, TE_{230}, and TE_{320} modes. Two sets of orthogonal radiation modes with the potential to produce dual-band circular polarization are the (TE_{120}, TE_{210}) modes at 3.82 GHz and the (TE_{130}, TE_{310}) modes at 5.4 GHz as indicated by the framed red triangles. The former set establishes the first passband, while the latter set is expected to support the second passband. There is another pair of

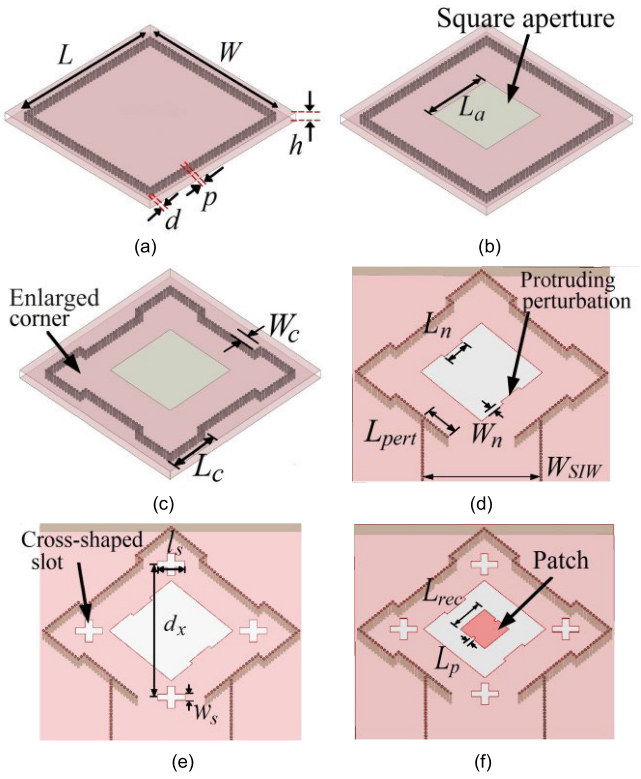

FIGURE 1. Development of the design for Antenna I: (a) the SIWC structure, (b) creating a square aperture, (c) enlarging the cavity corners, (d) introducing protruding perturbations and a SIW feed, (e) producing cross-shaped slots, and (f) adding a patch. The dimensions are: $L = W = 60$, $p = 1.5$, $d = 1$, $h = 3.18$, $L_a = 32$, $L_c = 18$, $W_c = 3$, $L_n = 9.8$, $W_n = 1.35$, $L_{pert} = 12$, $W_{SIW} = 44$, $l_s = 10$, $W_5 = 1.4$, $d_x = 60$, $L_{reg} = 12.8$, $L_p = 1$; all in mm.

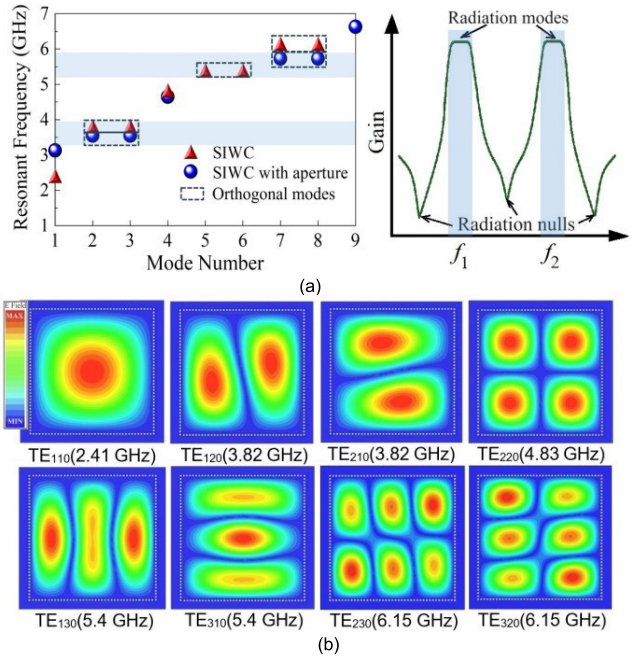

FIGURE 2. (a) Resonant frequency versus mode number of the proposed SIWC. Schematic diagram of the dual-band filtering gain response. (b) Electric field distributions of the Mode1-Mode8 in an order of their resonant frequencies from low to high.

orthogonal radiation modes (TE_{230}, TE_{320}) with the resonant frequency observed at 6.15 GHz, warranting further analysis to assess their impact on filtering response. The TE_{110} and TE_{220} modes resonate at 2.41 and 4.83 GHz, respectively, and both serve to generate radiation nulls for better rejection performance. A schematic diagram of the dual-band filtering gain response is illustrated in Fig. 2(a).

Figs. 1(a)−(f) illustrate the development of the antenna design. The configuration of the SIWC-backed square aperture is depicted in Fig. 1(b). The square aperture is located at the center of top surface to allow radiation from the SIWC. The aperture also benefits the transformation of the TE_{110} and TE_{220} modes into radiation nulls to improve rejection bandwidth [17]. The introduction of the aperture leads to changes in modal patterns. The TE_{120} and TE_{210} modes designed for the first passband do not vary significantly, while the TE_{130} and TE_{310} modes expected for the second passband disappear. The TE_{230} and TE_{320} modes still exist, however, their field distributions are altered, as shown in Figs. 3(a) and 3(b). They are referred to as the quasi-TE_{230} and quasi-TE_{320} modes with their resonant frequencies decreased to 5.73 GHz as indicated by the framed blue circles in Fig. 2(a), close to the center frequency of the second passband, and therefore contribute to that band. The aperture also increases the resonant frequency of the TE_{110} mode to 3.13 GHz and slightly reduces the resonant frequency of the TE_{220} mode to 4.65 GHz. In addition, a TE_{330} mode (Mode9) shown in Figs. 2(a) and 3(c) resonating at 6.63 GHz can produce a radiation null near the high end of the second passband, enhancing rejection level.

The feed for circular polarization must be placed at locations along the diagonal regions of the SIWC, where the electric fields of the two orthogonal modes appear to be strong for efficient excitation. However, Figs. 3(a) and 3(b) show the altered patterns of the quasi-TE_{230} and quasi-TE_{320} modes, indicating weak electric fields in the diagonal regions of the cavity. A solution to this problem is to enlarge the four SIWC corners to readjust their field distributions. The configuration of the SIWC with four enlarged corners is shown in Fig. 1(c), and the consequent changes of the modal patterns are displayed in Fig. 4. The figures show the field distributions of the TE_{230} and TE_{320} modes are back to normal, suitable for the second passband design. The field distributions of other modes present no significant changes, with only slight shifts in their resonant frequencies.

The increment of the aperture length (L_a) increases the frequencies of all resonant modes, as illustrated in Fig. 5, in which the change of the TE_{110} mode is the most significant. The figure also shows that when L_a exceeds 38 mm, the resonant frequency of the TE_{110} mode becomes quite close to the resonant frequencies of the TE_{120} and TE_{210} modes supporting the first passband. Since the TE_{110} mode serves to produce a radiation null near the low end of the first passband,

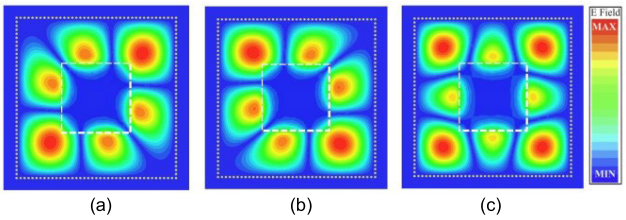

FIGURE 3. Electric field distributions of the SIWC with a created square aperture as in Fig. 1(b) and $L_a = 28$mm at various modes: (a) quasiTE_{230} mode of 5.73 GHz, (b) quasi- TE_{320} mode of 5.73 GHz, and (c) TE_{330} mode of 6.63 GHz.

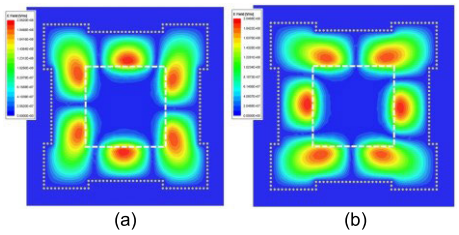

FIGURE 4. Electric field distributions of the SIWC with corners enlarged at 5.7 GHz: (a) TE_{230} mode and (b) TE_{320} mode.

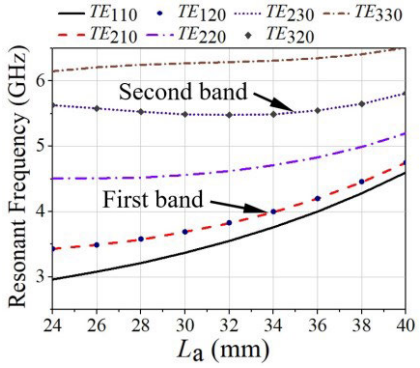

FIGURE 5. Variations of the resonant frequency of each mode subject to the changes in the aperture length L_a.

the value of L_a should not be too large to jeopardize the passband. The resonant frequency of the TE_{220} mode for the second radiation null is managed to locate between the two passbands, allowing it to increase the in-between rejection. Therefore, this frequency should not be too far away from the center frequencies of the two passbands. Fig. 5 also indicates that a value of L_a between 30 and 34 mm can ensure a reasonable distance between the resonant frequencies of the TE_{330} mode for the third radiation null and the second passband. A comprehensive assessment suggests that the proper values for L_a, W_c, and L_c be 32, 3, and 18 mm, respectively.

B. IMPLEMENTATION OF CP FILTERING RESPONSE IN THE FIRST BAND

The circular polarization property of this antenna design relies on the simultaneous excitation of two orthogonal modes with a phase difference of 90°. To achieve that, the feed point must locate at the diagonal region of the SIWC. An SIW feed line in the TE_{10} mode with a cutoff frequency at 2.4 GHz was proposed for the design. The width of the feed line W_{SIW} was determined to be 44 mm. Moreover, the resonant frequencies of the TE_{120} and TE_{210} modes are identical, which requires the introduction of perturbations to alter current paths and to effectively excite the two orthogonal modes. Fig. 1(d) depicts the structure for exciting circular polarization. The protruding perturbations are located at the opposite sides of the aperture, where the electric fields of the TE_{120} mode are the strongest and those of the TE_{210} mode are the weakest, facilitating the excitation of these two orthogonal modes. Since the protruding perturbations alter the lengths of the current paths, the resonant frequency of the TE_{120} mode is slightly lower than that of the TE_{210} mode.

Fig. 6 shows the electric field distributions as a function of time period at 3.72 GHz. When the time is equal to a quarter of a period (T), the electric field rotates 90° counterclockwise, presenting right-hand circular polarization (RHCP). The optimized impedance and axial-ratio bandwidths can be obtained by adjusting the length and width of the protruding perturbations. Fig. 7 demonstrates the excitation of the TE_{110} mode at 3.25 GHz. Taking the center of the SIWC as the coordinate origin, the current distributions on its top surface in this mode exhibit odd symmetry, resulting in radiation nulls due to field cancellation at far field.

An analysis on the width W_n of the protruding perturbations was conducted. Fig. 8 illustrates the simulation results for the $|S_{11}|$ and axial ratio (AR) responses. As the length of W_n decreases, the distance between the resonant frequencies

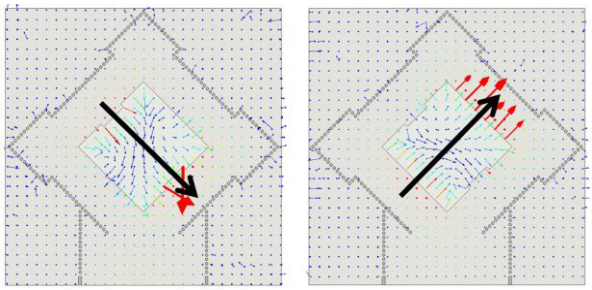

FIGURE 6. Changes of the Electric field distributions in time at 3.72 GHz: (a) $t = 0$ and (b) $t = T/4$.

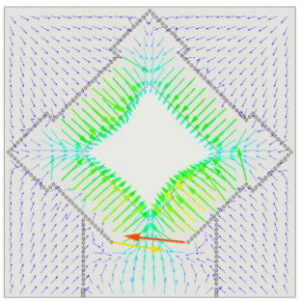

FIGURE 7. Surface current distribution of the TE_{110} mode at 3.25 GHz.

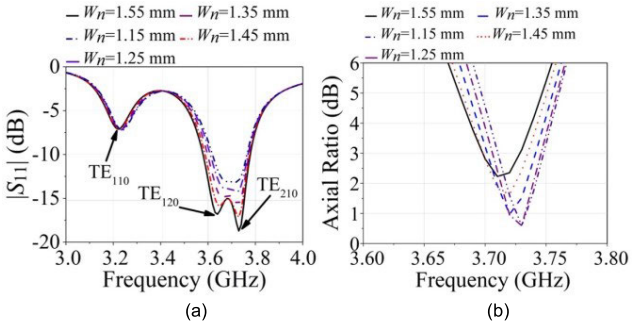

FIGURE 8. Simulated responses subject to the changes in the width of protruding perturbations, W_n: (a) $|S_{11}|$ and (b) AR.

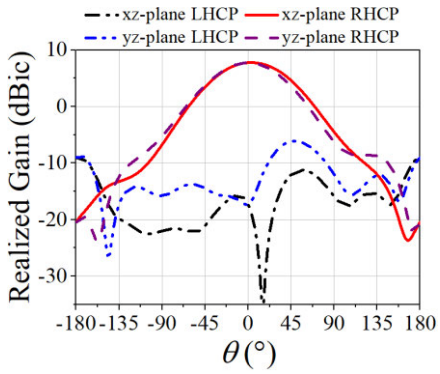

FIGURE 9. Simulated radiation patterns of the CP filtering antenna at 3.72 GHz.

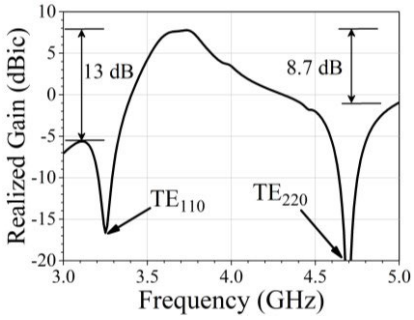

FIGURE 10. Simulated gain response of the antenna in the first band.

of the TE_{120} and TE_{210} modes decreases, leading to a narrower bandwidth and higher level of $|S_{11}|$, while the AR bandwidth becomes wider. On the contrary, increasing W_n results in a wider $|S_{11}|$ bandwidth but a narrower AR bandwidth, thus losing the CP performance. A compromised value for W_n is 1.35 mm. According to the analysis, L_n exhibits a relatively minor impact on the performance above and can serve as an auxiliary parameter to W_n for optimization. The value of L_n was chosen to be 9.8 mm. The simulated 10-dB impedance bandwidth ranges from 3.6 to 3.77 GHz or 4.61%, and the 3-dB AR bandwidth is from 3.7 to 3.74 GHz or 1.08%. Fig. 9 shows the radiation pattern at 3.72 GHz, with a peak gain of 7.76 dBic and a cross polarization of −25.04 dBic.

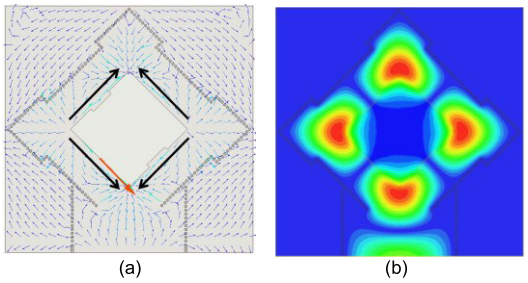

FIGURE 11. (a) Surface current and (b) electric field distributions of the antenna under the TE_{220} mode at 4.69 GHz.

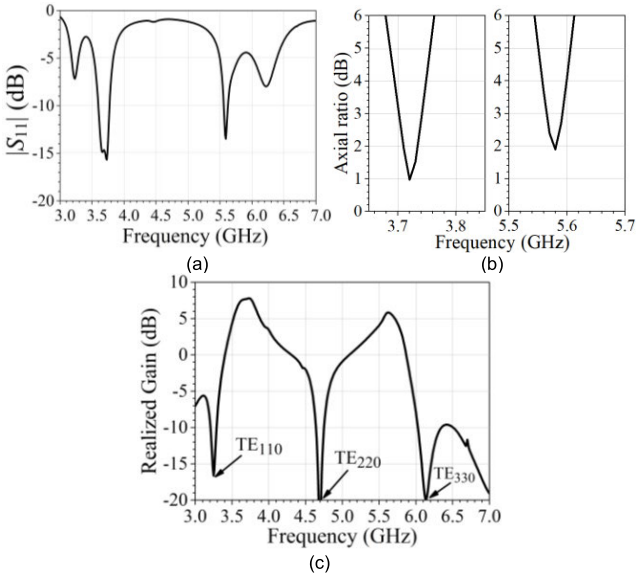

FIGURE 12. Performance of the antenna from Section II-B at further higher frequencies: (a) $|S_{11}|$, (b) AR, and (c) realized gain.

The simulated gain response is displayed in Fig. 10. The TE_{110} mode presents a rejection level of −13 dB near the lower frequency end, whereas the TE_{220} mode produces a rejection level of −8.7 dB near the higher frequency end, or at 4.69 GHz to be exactly. Figs. 11(a) and 11(b) show the surface current and electric field distribution in the TE_{220} mode, respectively. Since the directions of the surface currents near the opposite sides of the aperture are reverse to each other, a radiation null is expected to be in the boresight direction. However, since its resonant frequency is far away from the passband, the filtering effect is limited.

C. DESIGN OF DUAL-BAND CP FILTERING ANTENNA

Fig. 12 extends the analysis to the high-frequency performance of the antenna exploited in Section II-B. A resonant pole is observed near 5.6 GHz in the simulated $|S_{11}|$ response. The eigenmode analysis indicates that this resonant pole is generated by the TE_{230} and TE_{320} modes, and could contribute to the second passband. Figs. 13(a) and 13(b) show the electric field distributions of the TE_{230} and TE_{320} modes. However, the design on the aperture and protruding

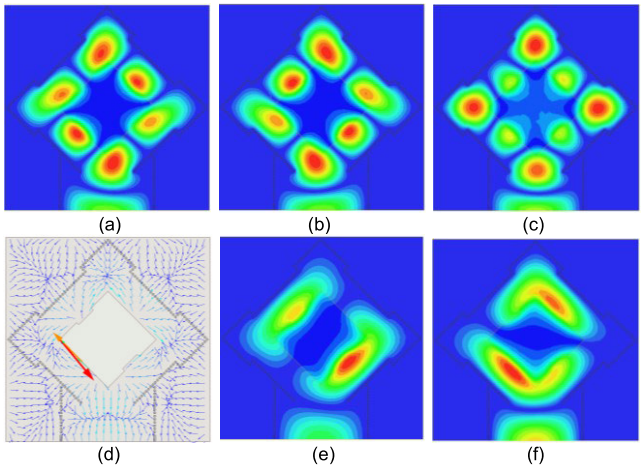

FIGURE 13. Electric field and surface current distributions in various modes: (a) TE_{230} of 5.62 GHz, (b) TE_{320} of 5.56 GHz, (c) TE_{330} of 6.14 GHz, (d) TE_{330} of 6.14 GHz, (e) TE_{120} of 3.66 GHz, and (f) TE_{210} of 3.72 GHz.

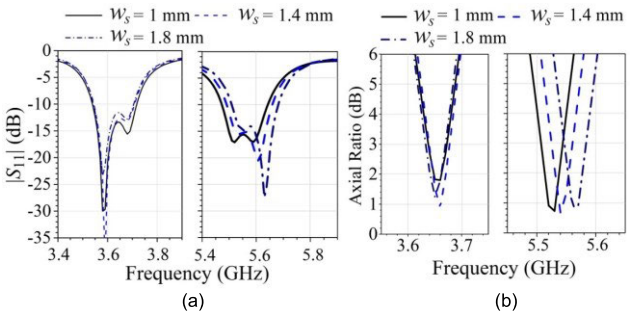

FIGURE 14. Variations of the simulated frequency responses subject to the changes in the slot width w_s: (a) $|S_{11}|$ and (b) AR.

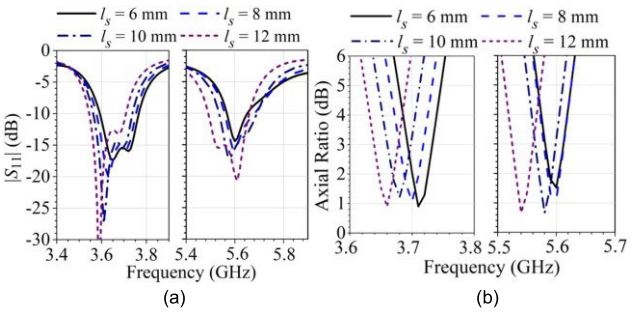

FIGURE 15. Variations of the simulated frequency responses subject to the changes in the slot length l_s: (a) $|S_{11}|$ and (b) AR.

perturbations from the previous subsection was exclusively developed for the first passband, its performance at the second passband is expected to be discouraging. The current design only exhibits an impedance bandwidth from 5.56 to 5.62 GHz or 1.07% and an AR bandwidth from 5.57 to 5.59 GHz or 0.39% for the second passband, indicating that more work is required.

A radiation null generated by the TE_{330} mode is observed at 6.14 GHz in Fig. 12(c). The corresponding electric field and surface current distributions are illustrated in Figs. 13(c) and 13(d), respectively. The current distribution in the TE_{330} mode also exhibits odd symmetry like the TE_{110} and TE_{220} modes, leading to a radiation null. The TE_{110}, TE_{220}, and TE_{330} modes create their own radiation nulls at the lower, middle, and upper stopbands, respectively, thus establishing a desired dual-band filtering response.

To increase the bandwidth of the second passband, slots can be arranged at places where the electric fields in the TE_{230} and TE_{320} modes are strong. These locations should not be anywhere near the areas where the electric fields in the TE_{120} and TE_{210} modes are strong in order not to jeopardize the performance of the first passband. Figs. 13(e) and 13(f) show that the electric fields in the two modes for the first passband are strong near the edge of the square aperture, while the electric fields at the corners of the SIWC are relatively weak. On the other hand, the main electric fields of the TE_{230} and TE_{320} modes of the second passband are distributed at the four corners of the cavity, as shown in Figs. 13(a) and 13(b), which make the ideal locations for the slots without affecting the first passband.

According to the above analysis, cross-shaped slots at the four corners of the SIWC are introduced in our design, as shown in Fig. 1(e), with a distance d_x of 60 mm between the diagonal slots. Reasonable values for the width w_s and length l_s of the slots were analyzed separately. Fig. 14 shows the responses of the simulated $|S_{11}|$ and AR as a function of the value of w_s while the value of l_s is fixed at 12 mm. Increasing the value of w_s will slightly shift the center frequency of the second passband to higher frequencies. The AR bandwidths of both passbands remain unchanged. A reasonable value of 1.4 mm was chosen for w_s. The analyzes on l_s with the value of w_s fixed at 1.4 mm is illustrated in Fig. 15. Decreasing the value of l_s doesn't substantially change the $|S_{11}|$ bandwidth in the first passband, but narrows the impedance and AR bandwidths of the second passband. A compromised value of 10 mm was selected for l_s. With the values selected, the simulation results show an impedance bandwidth from 3.56 to 3.74 GHz or 4.93%, and an AR bandwidth from 3.66 to 3.7 GHz or 1.08% for the first passband; as well as an impedance bandwidth from 5.53 to 5.69 GHz or 2.85%, and an AR bandwidth from 5.56 to 5.6 GHz or 0.72% for the second passband.

Fig. 16 compares the antenna gains with and without the cross-shaped slots. It's observed that the introduction of the cross-shaped slots increases the bandwidth of the second passband, however, it also degrades the rejection level near the higher end of the passband, down to 12.2 dB only. Therefore, more radiation nulls were required to solve this problem.

A square patch was introduced and placed at the center of the aperture, as shown in Fig. 1(f), to solve the problem above. There exists both electric and magnetic coupling between the SIWC-backed aperture and the embedded patch, which establish a mixed coupling structure. According to the coupling theory from filter designs, transmission zeros can be generated by canceling electric and magnetic couplings out to

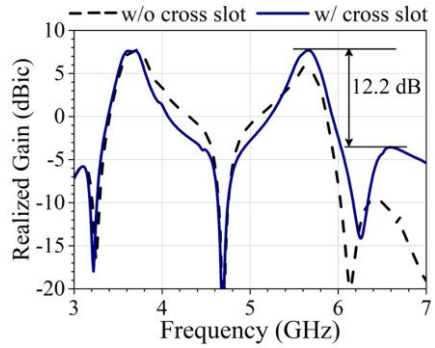

FIGURE 16. Comparison on the simulated gain responses of the SIWC with and without the cross-shaped slots.

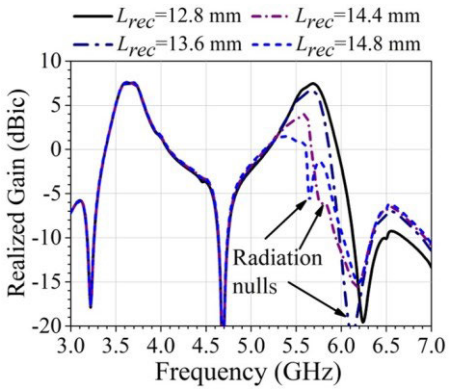

FIGURE 17. Variations of the simulated gain responses subject to the changes in the patch length L_{rec}.

enhance selectivity and rejection level [21], [22]. To preserve the original circular polarization property of the aperture and to avoid interference from the patch, notch perturbations were presented to the patch to excite its TM_{01} and TM_{10} orthogonal modes, which correspond to the TE_{230} and TE_{320} modes of the original cavity.

Fig. 17 illustrates the simulated gain responses subject to four values for the patch length L_{rec}. The first passband is almost unaffected with respect to the presence of the patch, while noticeable radiation nulls appear near the second passband. By adjusting L_{rec}, the radiation nulls generated by the patch are brought close to the TE_{330} null of the cavity, improving stopband rejection. The final values for L_{rec} and L_p are 12.8 and 1 mm, respectively, which increase the stopband rejection from 12.2 dB to 17 dB.

Fig. 18 shows the 3D view and photographs of Antenna I. The SIW input port was extended to include a GCPW-to-SIW transition for measurements. Fig. 19 illustrates the $|S_{11}|$, AR, and gain responses of Antenna I. The measured impedance bandwidth of the first passband ranges from 3.59 to 3.78 GHz or 5.16% in contrast to the simulated one from 3.57 to 3.74 GHz or 4.65%. The measured AR bandwidth is from 3.67 to 3.71 GHz or 1.1% compared to the simulated one from 3.65 to 3.69 GHz or 1.09%. The measured impedance bandwidth of the second passband is from 5.56 to 5.76 GHz or

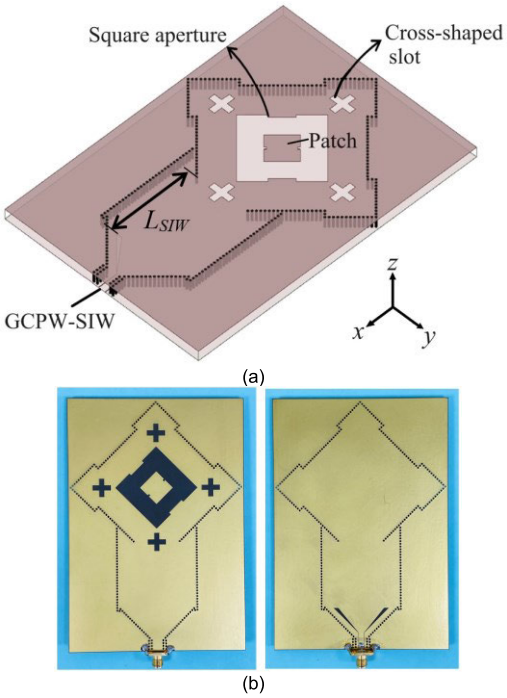

FIGURE 18. Antenna I: (a) 3-D view, (b) photographs. (L_{SIW} = 37 mm).

3.53%, whereas the simulated one is from 5.54 to 5.76 GHz or 3.89%. The measured AR bandwidth of the second passband ranges from 5.58 to 5.64 GHz or 1.07% in comparison with the simulated one from 5.58 to 5.62 GHz or 0.71%. The measured stopband rejection levels are more than 23 dB near the lower end of the first passband, more than 10 dB between the two passbands, and more than 17 dB near the higher end of the second passband. Figs. 20(a) and 20(b) show the measured radiation patterns at 3.7 and 5.6 GHz from the two passbands, with the peak gain values of 7.1 and 6.97 dBic, respectively.

III. DUAL-BAND CP FILTERING ANTENNA WITH THREE CSRRs (ANTENNA II)

Complementary Split-Ring Resonator (CSRR) is a structure commonly used in metamaterials [23], [24], [25], [26], [27]. It can be excited by electric fields parallel to the axis of the ring, generating a steep rejection band. A typical CSRR structure employs a set of two concentric split rings, with their openings in opposite directions, and the length of the outside ring approximately equal to half of the guided wavelength. This work uses a single square split-ring slot as a CSRR unit, which is simpler in design.

First, a single CSRR is introduced to the SIW feedline alone to evaluate its filtering performance. The CSRR is fabricated at the bottom metal layer, as shown in Fig. 21(a). The width of the SIW line, W_{SIW}, is set to 44 mm as in Antenna I. Fig. 21(b) shows the equivalent circuit of the SIW line loaded by a single CSRR, where L_d and C_d are the inductance and capacitance effects of the SIW line, the capacitive coupling

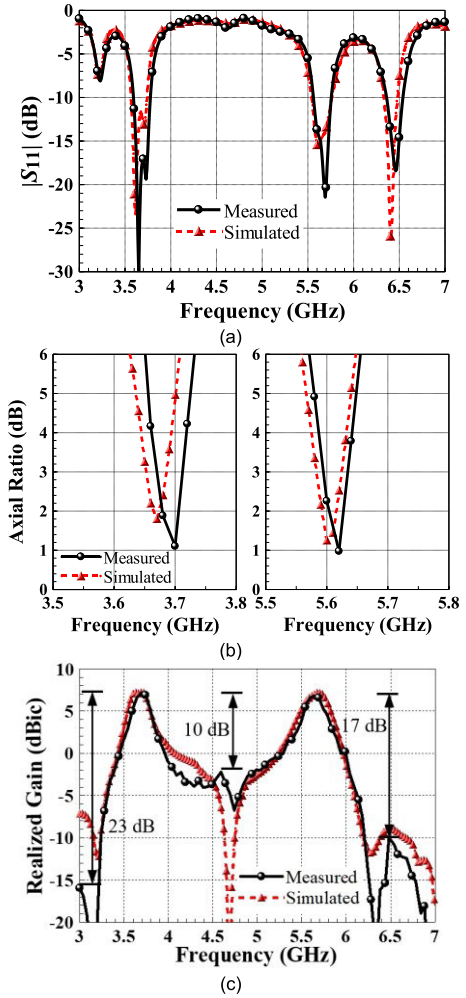

FIGURE 19. Comparison on the measured and simulated (a) $|S_{11}|$ response, (b) AR, and (c) realized gain of Antenna I.

between the CSRR and SIW is denoted by C_c, and the CSRR is modeled by means of the shunt-connected resonant tank consisting of L_r and C_r. Fig. 21(c) compares the full-wave and circuit simulations of the proposed equivalent circuit, and the results are in good agreement.

The value of L_r is mainly determined by the perimeter length of the CSRR, while C_r primarily depends on the width of the slot, b. The resonant frequency of a CSRR can be estimated by the approximate equation:

$$f_r = \frac{c_v}{2\left[4\left(a-b\right)-c\right]\sqrt{\frac{\varepsilon_r+1}{2}}} \tag{2}$$

where c_v is the speed of light. The design of Antenna I gives the center frequency of the middle stopband approximately equal to 4.7 GHz, which allows to seek for the initial dimensions of the CSRR via (2).

A. ANALYSIS OF CSRR

Figs. 22(a)–(c) demonstrate the analysis on the dimensions of the CSRR, namely a, b, and c, respectively. The simulation

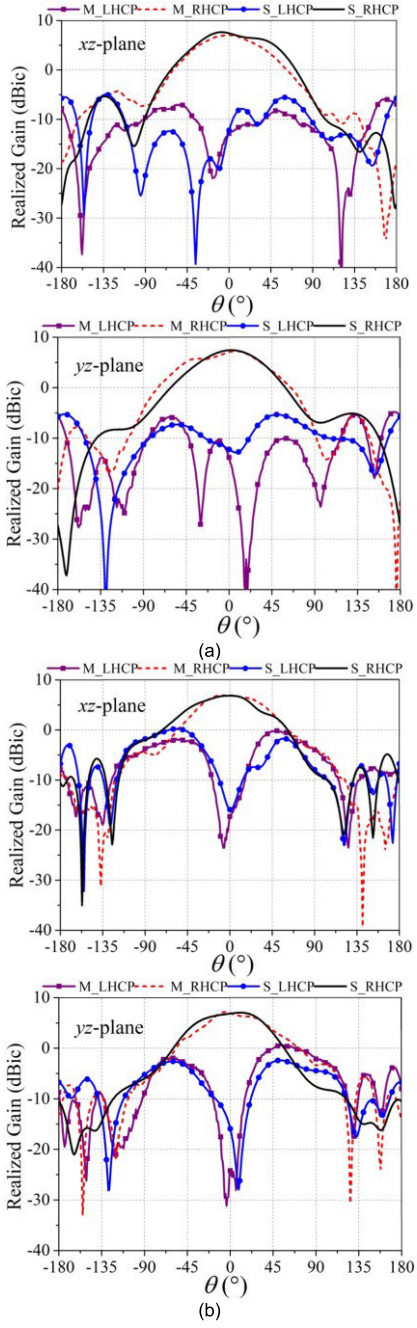

FIGURE 20. Comparison on the measured and simulated radiation patterns of Antenna I at (a) 3.7 GHz and (b) 5.6 GHz.

results show a transmission zero near 4.7 GHz, but the bandwidth is very narrow. Increasing the value of a results in a larger equivalent inductance, which shifts the resonant point to a lower frequency. A wider b results in a smaller equivalent capacitance, thus shifting the resonant frequency to a higher frequency and slightly lowering the level. A larger c reduces the equivalent inductance, thereby shifting the resonant frequency to a higher frequency. The final dimensions are set to be 7.6, 1, and 1.1 mm for the values of a, b, and c, respectively. From the above analysis, the dimensions of the CSRR show

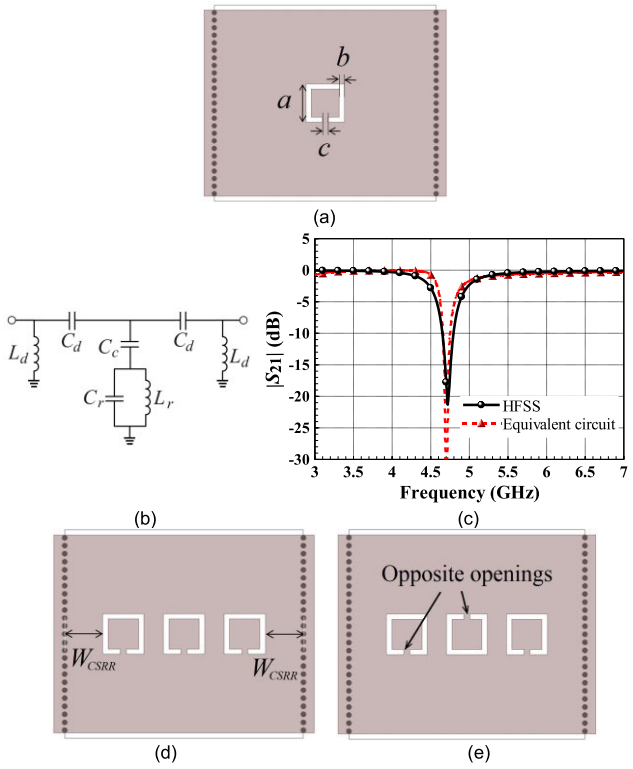

FIGURE 21. (a) Configuration of a single CSRR-loaded SIW line. (b) Equivalent circuit of Fig. 21(a). (c) Simulated responses of the equivalent circuit with $L_d = 1.7$ nH, $C_d = 1.9$ pF, $C_c = 0.35$ pF, $L_r = 1.25$ nH, and $C_r = 0.55$ pF. (d) Three CSRRs with their openings in the same direction. (e) Three CSRRs with the openings of the adjacent ones opposite to each other.

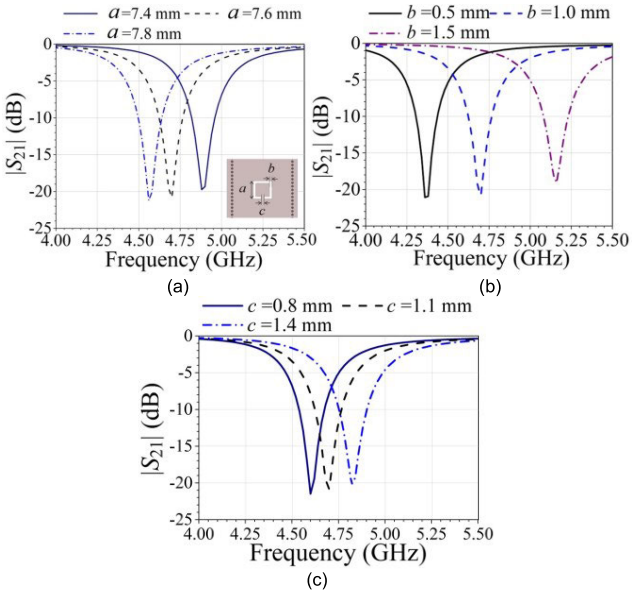

FIGURE 22. Variations of the simulated $|S_21|$ responses of a single CSRR subject to the changes in the following: (a) parameter a with $b = 1$ and $c = 1.1$ mm, (b) parameter b with $a = 7.6$ and $c = 1.1$ mm, (c) parameter c with $a = 7.6$ and $b = 1$ mm.

little impact on the 3-dB $|S_{21}|$ bandwidth, which always stays around 9.5% (4.47−4.92 GHz). Thus, a single CSRR fails to

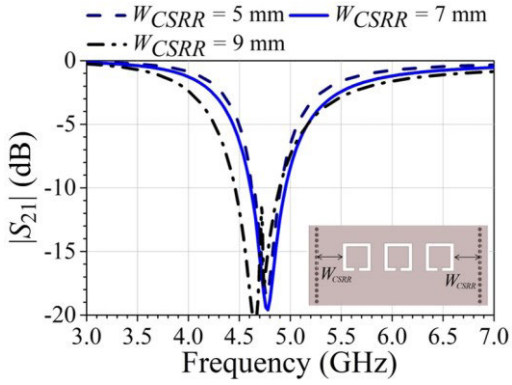

FIGURE 23. Simulated $|S_{21}|$ responses of the three CSRRs from Fig. 21(d) with $a = 7.6$, $b = 1$, and $c = 1.1$, all in mm.

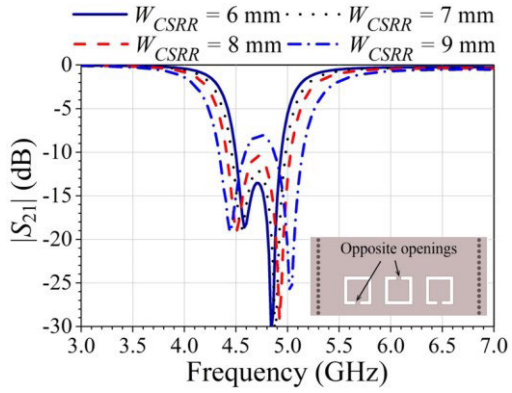

FIGURE 24. Simulated $|S_{21}|$ responses of the three CSRRs from Fig. 21(e).

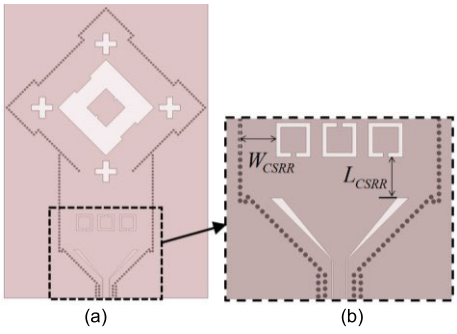

FIGURE 25. Configuration of the antenna with three coplanar CSRRs: (a) top view, (b) partial bottom view.

cover the entire middle stopband, and its contribution to the rejection level is trivial.

Multiple CSRRs were proposed to solve the above problem of inadequate bandwidth [24]. Conventionally, these CSRRs are generally aligned along the SIW line. However, considering the limited length of the SIW feedline for Antenna I, the longitudinal arrangement would leave the last CSRR too close to the SIWC, causing unnecessary interference. Therefore, the CSRRs were placed transversely to the SIW.

Fig. 21(d) shows the distribution of three coplanar CSRRs, with their openings in the same direction. The distance

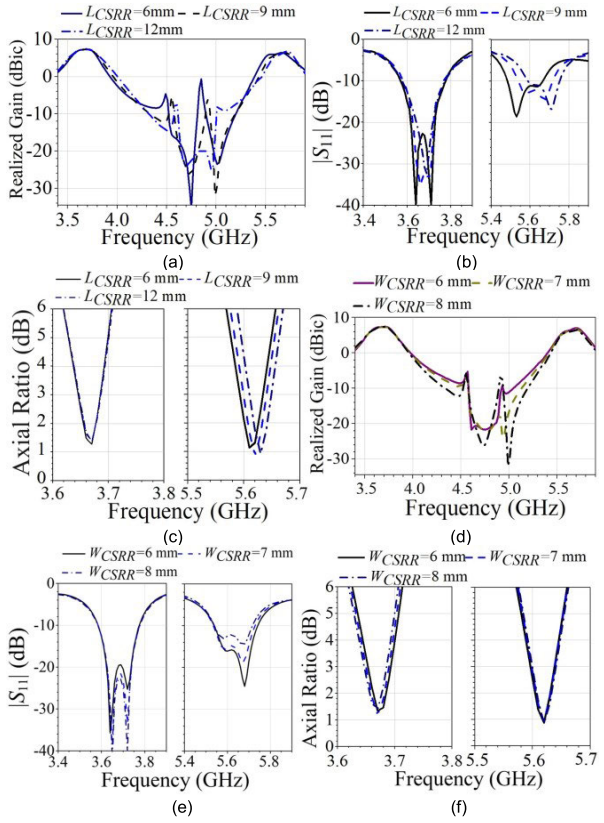

FIGURE 26. Simulated responses of the antenna subject to the changes in the parameters of the three coplanar CSRRs. Responses to the changes in L_{CSRR}: (a) realized gain, (b) $|S_{11}|$, and (c) AR. Responses to the changes in W_{CSRR} : (d) realized gain, (e) $|S_{11}|$, and (f) AR.

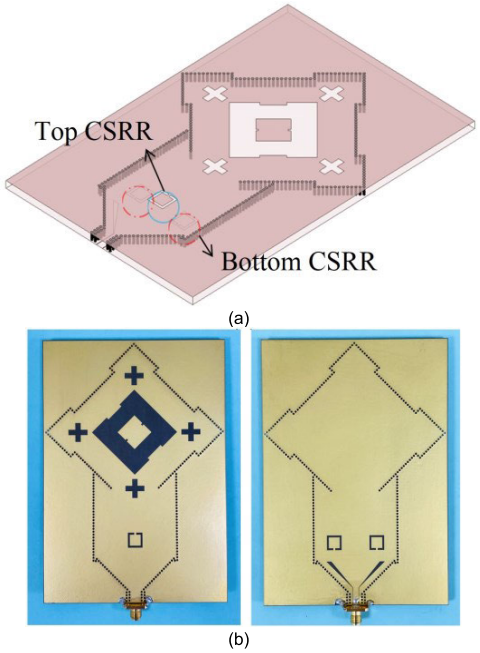

FIGURE 27. Antenna II with the CSRRs at upper and lower metal layers: (a) 3-Dview, (b) photographs. The values of the design parameters are: $a = 7.7, b = c = 1, L_{CSRR} = 6, W_{CSRR} = 7$, all in mm.

between the edge of the side CSRR and the via wall is denoted as W_{CSRR}. The dimensions of each CSRR remain the

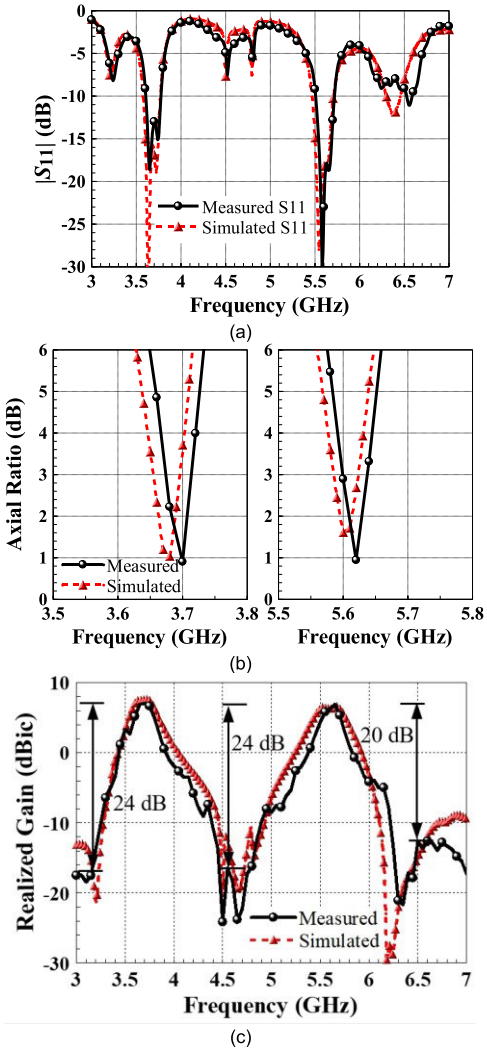

FIGURE 28. Comparison on the measured and simulated (a) $|S_{11}|$ response, (b) AR, and (c) realized gain of Antenna II.

same as those for a single CSRR. The performance of these CSRRs subject to the variations of the distance W_{CSRR} are illustrated in Fig. 23. As the value of W_{CSRR} increases, the two adjacent CSRRs are closer to each other with stronger mutual coupling, leading to a wider bandwidth. The value of 9 mm for W_{CSRR} offers a 3-dB $|S_{21}|$ bandwidth from 4.08 to 5.46 GHz or 28.93%, which is more than three times wider than a single CSRR. However, the insertion loss great than 2.5 dB over the frequency range (5.56−5.76 GHz) of the second passband would cost the antenna gain.

The above problem of poor insertion loss can be solved if the opening of the middle CSRR is in the opposite direction to its two adjacent CSRRs, as shown in Fig. 21(e). Fig. 24 shows the simulated $|S_{21}|$ response of the three CSRRs with the specified openings. Two resonant poles are observed from the figure. As the value of W_{CSRR} increases, the 3-dB bandwidth becomes wider. The value of 8 mm for W_{CSRR} provides a 3-dB bandwidth from 4.3 to 5.15 GHz or 18%, and the insertion

TABLE 1. Comparison With Previous Filtering Antennas and Dual-Band Antennas.

Ref.	Operating freq. & IPBW (%)	Pol.	AR bandwidth	Filtering response	Number of nulls	Peak Gain	Rejection level	Element number	Number of layers	Extra filters
[10]	11.8 GHz, 11.84%	LP	NA	Yes	2	5 dBi	*LS: 6.6 dB *US: 15.3 dB	1	1	No
[13]	9.56 GHz, 2.53%	LP	NA	Yes	2	5.8 dBi	*LS: 12.3 dB *US: 9.7 dB	1	1	No
[14]	3.5 GHz, 9.14%	LP	NA	Yes	2	7.3 dBi	LS: 15.2 dB US: 15 dB	1	1	No
[15]	10.19 GHz, 7.6%	RHCP	9.9–10.03 GHz, 1.3%	Yes	No	6.77 dBic	*LS: 46 dB *US: 27 dB	1	3	Yes
[17]	10 GHz, 21%	RHCP	9.15–10.95 GHz, 18%	Yes	4	13.2 dBic	LS: 33 dB US: 23 dB	2×2	2	No
[18]	2.51 GHz, 15% 5.38 GHz, 23%	LHCP RHCP	2.39–2.57 GHz, 7.3% 5.13–6 GHz, 15.6%	No	No	2.48 dBic 3.09 dBic	NA	1	1	No
[19]	2.91 GHz, 18.6% 5.41 GHz, 10.9%	RHCP RHCP	*2.8–2.89 GHz, 3.2% *5.17–5.31 GHz, 2.7%	No	No	4.79 dBic 4.27 dBic	NA	1	1	No
[20]	2.45 GHz, 1.8% 5.8 GHz, 2.3%	LHCP LHCP	*2.37–2.52 GHz, 6% *5.7–5.85 GHz, 2.5%	Yes	No	0 dBic 1.5 dBic	*LS: 12 dB MS: NP *US: 7.8 dB	1	4	Yes
Antenna I	**3.69 GHz, 5.16% 5.66 GHz, 3.53%**	**RHCP, RHCP**	**3.67–3.71 GHz, 1.1%, 5.58–5.64 GHz, 1.07%**	**Yes**	**3**	**7.1 dBic 6.97 dBic**	**LS: 23 dB MS: 10 dB US: 17 dB**	**1**	**1**	**No**
Antenna II	**3.7 GHz, 4.6% 5.62 GHz, 3.74%**	**RHCP, RHCP**	**3.68–3.71 GHz, 0.81%, 5.6–5.64 GHz, 0.71%**	**Yes**	**3**	**7.78 dBic 6.73 dBic**	**LS: 24 dB MS: 24 dB US: 20 dB**	**1**	**1**	**No**

Operating freq. = Operating frequency, IPBW = Impedance bandwidth, Pol. = Polarization, LS = Lower stopband, MS = Middle stopband, US = Upper stopband, NP = not provided, NA = Not available, *= Calculated from the graph of the referenced paper.

loss over the frequency range of the second passband is less than 0.9 dB. The above simulation results indicates that the three CSRRs at the feed line can effectively improve the middle stopband performance of Antenna I.

B. DUAL-BAND CP FILTERING ANTENNA WITH THREE CSRRs

Fig. 25 shows the configuration of the antenna with three CSRRs from Fig. 21(e), where L_{CSRR} is the distance between the bottom edge of the CSRR and the top of the GCPW slot. Figs. 26(a)–(c) examine the performance of the antenna from Fig. 25 subject to the variations of the parameter L_{CSRR}. From the gain curves in Fig. 26(a), surges appear at around 4.5 GHz and 4.9 GHz. The addition of the antenna structure will affect the electric field distribution of the SIW line, resulting in incorrect excitation of the CSRR and causing additional resonance. Changing the value of L_{CSRR} can slightly reduce the surges and improve the $|S_{11}|$ level in the second passband. A suitable value of 9 mm is recommended for L_{CSRR} according to the results from Figs. 26(a) and 26(b). Fig. 26(c) shows the parameter L_{CSRR} has little impact on the AR bandwidth. The influence of the parameters W_{CSRR} is explored in Figs. 26(d)–(f). By setting the value of W_{CSRR} equal to 7 mm, the level of the surge near 4.9 GHz in the gain curve is reduced to below −16 dBic, although the one at 4.55 GHz remains at −7 dBic. The impedance and AR bandwidths are only slightly disturbed by the introduction of the CSRRs.

Through the non-coplanar configuration of the CSRR, the undesired resonances caused by the interaction between the CSRRs and Antenna I can be further reduced. The three CSRRs were all placed at the bottom metal layer of the SIW feed line in the early configuration. The new configuration relocates the middle CSRR to the top metal layer of the SIW feed line, while the other two CSRRs remain at the bottom metal layer, as demonstrated in Fig. 27. This final design is subsequently referred to as "Antenna II".

Fig. 28 shows the $|S_{11}|$ response, gain, and AR response of Antenna II. The original surges disappear in the gain plot, and the rejection level between the two passbands is enhanced by the new configuration of the CSRRs. The measurement results show that the impedance bandwidth of the first passband ranges from 3.61 to 3.78 GHz or 4.6% in comparison with the simulated bandwidth from 3.57 to 3.76 GHz or 5.18%, and the AR bandwidth is from 3.68 to 3.71 GHz or 0.81% in contrast to the simulated bandwidth from 3.65 to 3.69 GHz or 1.09%. For the second passband, the measured impedance bandwidth is from 5.51 to 5.72 GHz or 3.74%, whereas the simulated bandwidth is from 5.46 to 5.71 GHz or 4.48%. The measured AR bandwidth ranges from 5.6 to 5.64 GHz or 0.71% compared to the simulated bandwidth from 5.59 to 5.62 GHz or 0.54%. The measured rejection levels are greater than 24, 24, and 20 dB at the lower, middle, and upper stopbands, respectively. Figs. 29(a) and 29(b) show the measured radiation patterns at 3.7 GHz and 5.6 GHz, and the gain values of 7.78 and 6.73 dBic, respectively,

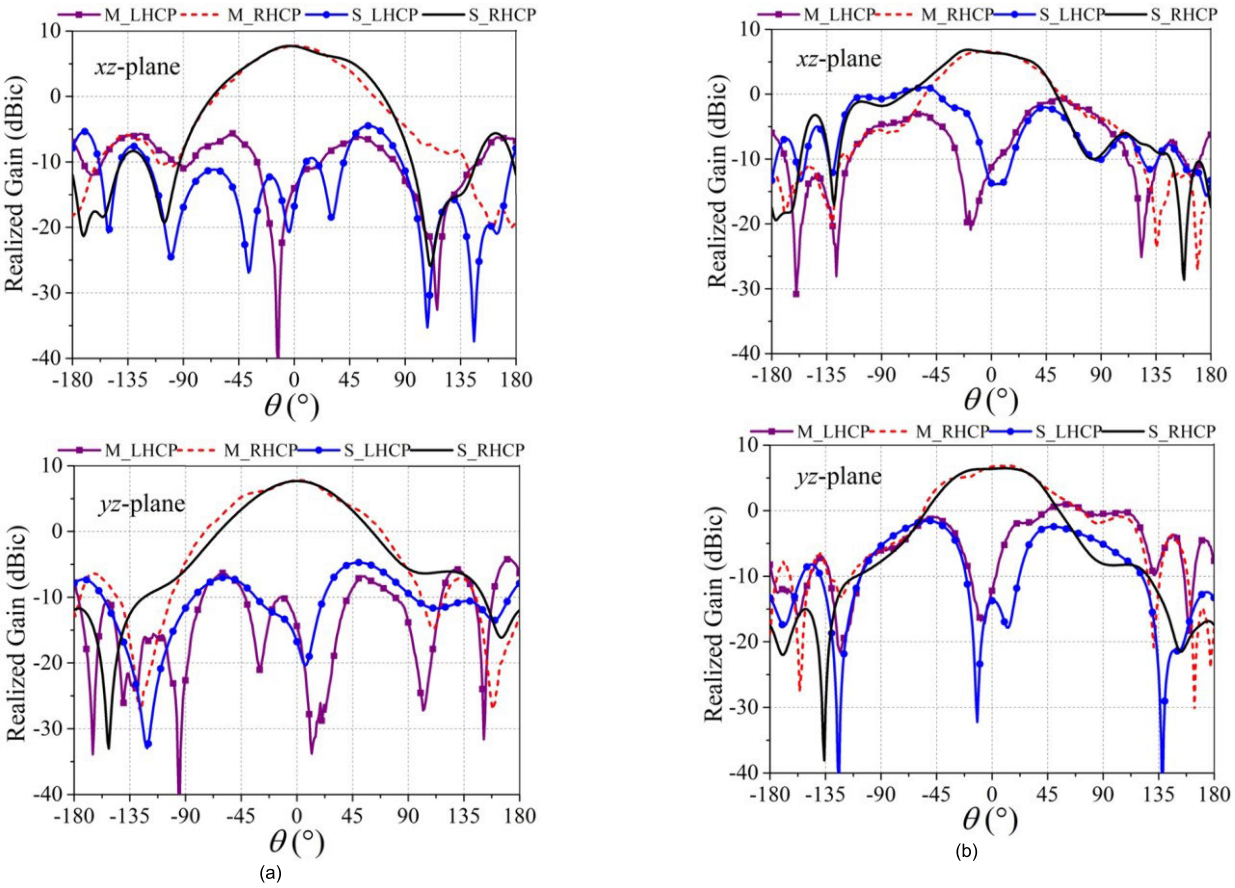

FIGURE 29. Comparison on the measured and simulated radiation patterns of Antenna II at (a) 3.7 GHz and (b) 5.6 GHz.

to represent the performance of Antenna II over the two passbands.

A comprehensive comparison is listed in Table 1, revealing that the proposed filtering antenna offers the features of single-layer structure, dual-band operation, circular polarization, rejection levels up to 24 dB, gain up to 7.78 dBic, and no additional filters required. Moreover, the presence of the radiation nulls contributes excellent selectivity on both sides of the two passbands.

IV. CONCLUSION

This work develops two SIWC-backed slot antennas (Antenna I and II), featuring single-layer, dual-band, circular polarization, and filtering characteristics, suitable for 5G NR n46 and n78 communication applications. Antenna I is characterized by a square aperture at the center and four cross slots at the corners of the SIWC top surface to excite two pairs of orthogonal radiation modes, TE_{120}/TE_{210} and TE_{230}/TE_{320}, respectively, to establish the first and second passbands, thus presenting the property of dual-band circular polarization. Excitation of other modes such as TE_{110}, TE_{220}, and TE_{330} results in radiation nulls to achieve filtering responses. To further enhance filtering performance, the design of Antenna II is proposed, where three CSRRs are introduced at the SIW feedline. Their wide stopband characteristic improves the rejection level. The middle CSRR is placed at a different metal layer of the SIW feed line from the one for the two side CSRRs to reduce undesired resonances. Measured data show that the gain value can reach up to 7.78 dBic. The filtering performance is excellent, with stopband rejection levels up to 24 dB.

REFERENCES

[1] H. Jin, G.-Q. Luo, W. Wang, W. Che, and K.-S. Chin, "Integration design of millimeter-wave filtering patch antenna array with SIW four-way anti-phase filtering power divider," *IEEE Access*, vol. 7, pp. 49804–49812, 2019.

[2] H. Chu, C. Jin, J.-X. Chen, and Y.-X. Guo, "A 3-D millimeter-wave filtering antenna with high selectivity and low cross-polarization," *IEEE Trans. Antennas Propag.*, vol. 63, no. 5, pp. 2375–2380, May 2015.

[3] P. F. Hu, Y. M. Pan, X. Y. Zhang, and S. Y. Zheng, "Broadband filtering dielectric resonator antenna with wide stopband," *IEEE Trans. Antennas Propag.*, vol. 65, no. 4, pp. 2079–2084, Apr. 2017.

[4] J. Wu, Z. Zhao, Z. Nie, and Q.-H. Liu, "A printed unidirectional antenna with improved upper band-edge selectivity using a parasitic loop," *IEEE Trans. Antennas Propag.*, vol. 63, no. 4, pp. 1832–1837, Apr. 2015.

[5] C.-T. Chuang, T.-J. Lin, and S.-J. Chung, "A band-notched UWB monopole antenna with high notch-band-edge selectivity," *IEEE Trans. Antennas Propag.*, vol. 60, no. 10, pp. 4492–4499, Oct. 2012.

[6] X. Y. Zhang, W. Duan, and Y.-M. Pan, "High-gain filtering patch antenna without extra circuit," *IEEE Trans. Antennas Propag.*, vol. 63, no. 12, pp. 5883–5888, Dec. 2015.
[7] W. Duan, X. Y. Zhang, Y.-M. Pan, J.-X. Xu, and Q. Xue, "Dual-polarized filtering antenna with high selectivity and low cross polarization," *IEEE Trans. Antennas Propag.*, vol. 64, no. 10, pp. 4188–4196, Oct. 2016.
[8] Y. Zhang, X. Y. Zhang, and Y.-M. Pan, "Compact single- and dual-band filtering patch antenna arrays using novel feeding scheme," *IEEE Trans. Antennas Propag.*, vol. 65, no. 8, pp. 4057–4066, Aug. 2017.
[9] S. J. Yang, Y. M. Pan, L.-Y. Shi, and X. Y. Zhang, "Millimeter-wave dual-polarized filtering antenna for 5G application," *IEEE Trans. Antennas Propag.*, vol. 68, no. 7, pp. 5114–5121, Jul. 2020.
[10] J.-Y. Yin, T.-L. Bai, J.-Y. Deng, J. Ren, D. Sun, Y. Zhang, and L.-X. Guo, "Wideband single-layer substrate integrated waveguide filtering antenna with U-shaped slots," *IEEE Antennas Wireless Propag. Lett.*, vol. 20, pp. 1726–1730, 2021.
[11] R. Wang, Y. Duan, Y. Song, W.-G. Zhao, Y.-H. Lv, M.-S. Liang, and B.-Z. Wang, "Broadband high-gain empty SIW cavity-backed slot antenna," *IEEE Antennas Wireless Propag. Lett.*, vol. 20, pp. 2073–2077, 2021.
[12] G. Qing Luo, Z. Fang Hu, L. Xi Dong, and L. Ling Sun, "Planar slot antenna backed by substrate integrated waveguide cavity," *IEEE Antennas Wireless Propag. Lett.*, vol. 7, pp. 236–239, 2008.
[13] C. Wang, X. Wang, H. Liu, Z. Chen, and Z. Han, "Substrate integrated waveguide filtenna with two controllable radiation nulls," *IEEE Access*, vol. 8, pp. 120019–120024, 2020.
[14] Q. Liu, L. Zhu, J. Wang, and W. Wu, "A wideband patch and SIW cavity hybrid antenna with filtering response," *IEEE Antennas Wireless Propag. Lett.*, vol. 19, pp. 836–840, 2020.
[15] T. Li and X. Gong, "Vertical integration of high-Q filter with circularly polarized patch antenna with enhanced impedance-axial ratio bandwidth," *IEEE Trans. Microw. Theory Techn.*, vol. 66, no. 6, pp. 3119–3128, Jun. 2018.
[16] W. Wang, H. Jin, W. Yu, X. H. Zhang, F. Wu, K.-S. Chin, and G. Q. Luo, "A single-layer dual-circularly polarized SIW-cavity-backed patch filtenna with wide axial-ratio bandwidth," *IEEE Antennas Wireless Propag. Lett.*, vol. 20, pp. 908–912, 2021.
[17] W. Wang, H. Jin, W. Yu, X. H. Zhang, K.-S. Chin, and G. Q. Luo, "A wideband circularly polarized 2×2 filtenna array with multiple radiation nulls," *IEEE Antennas Wireless Propag. Lett.*, vol. 21, pp. 595–599, 2022.
[18] M.-T. Tan and B.-Z. Wang, "A dual-band circularly polarized planar monopole antenna for WLAN/Wi-Fi applications," *IEEE Antennas Wireless Propag. Lett.*, vol. 15, pp. 670–673, 2016.
[19] Y. Xu, L. Zhu, and N.-W. Liu, "Design approach for a dual-band circularly polarized slot antenna with flexible frequency ratio and similar in-band gain," *IEEE Antennas Wireless Propag. Lett.*, vol. 21, pp. 1037–1041, 2022.
[20] Y. Qin, M. Han, L. Zhang, C.-X. Mao, and H. Zhu, "A compact dual-band omnidirectional circularly polarized filtering antenna for UAV communications," *IEEE Trans. Veh. Technol.*, vol. 72, no. 12, pp. 16742–16747, Dec. 2023.
[21] P. F. Hu, Y. M. Pan, K. W. Leung, and X. Y. Zhang, "Wide-/dual-band omnidirectional filtering dielectric resonator antennas," *IEEE Trans. Antennas Propag.*, vol. 66, no. 5, pp. 2622–2627, May 2018.
[22] R. J. Cameron, C. M. Kudsia, and R. R. Mansour, *Microwave Filters for Communication Systems: Fundamentals, Design and Applications*, 2nd ed., Hoboken, NJ, USA: Wiley, 2018.
[23] F. Martín, J. Bonache, F. Falcone, M. Sorolla, and R. Marqués, "Split ring resonator-based left-handed coplanar waveguide," *Appl. Phys. Lett.*, vol. 83, no. 22, pp. 4652–4654, Dec. 2003.
[24] F. Falcone, T. Lopetegi, J. D. Baena, R. Marques, F. Martin, and M. Sorolla, "Effective negative-ε stopband microstrip lines based on complementary split ring resonators," *IEEE Microw. Wireless Compon. Lett.*, vol. 14, no. 6, pp. 280–282, Jun. 2004.
[25] J.-A. Wang, D. Li, Y. Liu, Z. Chen, Z. Zheng, and Y. Deng, "Compact substrate integrated waveguide bandstop filter based on CSRRs," in *Proc. IEEE Asia–Pacific Microw. Conf. (APMC)*, Dec. 2020, pp. 222–224.
[26] Y. Dong and T. Itoh, "Miniaturized dual-band substrate integrated waveguide filters using complementary split-ring resonators," in *IEEE MTT-S Int. Microw. Symp. Dig.*, Baltimore, MD, USA, Jun. 2011, pp. 1–4.
[27] S. S. Karthikeyan and R. S. Kshetrimayum, "Notched UWB bandpass filter using complementary single split ring resonator," *IEICE Electron. Exp.*, vol. 7, no. 17, pp. 1290–1295, 2010.

CHENG-FANG CAO was born in Taipei City, Taiwan, in 1998. He received the B.S. degree in physics from National Taiwan Normal University, Taipei City, in 2020, and the M.S. degree in electronic engineering from National Taipei University of Technology, Taipei City, in 2022. His research interests include microwave circuits and antennas.

ERIC S. LI received the B.S. degree from Tamkang University, New Taipei City, Taiwan, in 1986, the M.S. degree in electrical engineering from the State University of New York, Stony Brook, NY, USA, in 1987, and the Ph.D. degree in electrical engineering from the University of Michigan, Ann Arbor, MI, USA, in 1998.

From 1988 to 1992 and from 1998 to 1999, he was with Wireless Industries as a Microwave Engineer participating in the designs of microwave circuits and antennas. From 1999 to 2006, he was a Faculty Member with the Department of Electrical Engineering, National Chi Nan University, Taiwan. Since 2006, he has been with the Department of Electronic Engineering, National Taipei University of Technology, Taiwan, where he is currently a Professor. His research interests include high-frequency circuits, high-frequency calibration and measurement techniques, microwave and millimeter-wave polarimetric radar systems, and electromagnetic scattering.

HUAYAN JIN (Member, IEEE) received the B.S. degree in electronic engineering and the Ph.D. degree in electromagnetic field and microwave technology from Nanjing University of Science and Technology (NUST), Nanjing, China, in 2011 and 2017, respectively. From 2012 to 2014, she went to Chang Gung University as an Exchange Student for academic exchange and study. Since 2017, she has been a Lecturer with the School of Electronics and Information, Hangzhou Dianzi University, Hangzhou, China, and was promoted to an Associate Professor, in 2021. Her main research interests include millimeter-wave antennas, shared-aperture antennas, differential-fed antennas, and filtering antennas.

DONGXU CHEN was born in Xuzhou, Jiangsu, China, in 1994. She received the B.Eng. and Ph.D. degrees from Nanjing University of Science and Technology (NUST), Nanjing, China, in 2015 and 2021, respectively.

In 2017, she was an Exchange Student with the Department of Electronics Engineering, Chang Gung University (CGU). Since 2021, she has been with the College of Computer and Information, Hohai University, Nanjing. Her main research interests include artificial material-based antenna arrays, metasurface antenna, millimeter-wave antenna arrays, and multi-functional antennas. She was a recipient of the Best Paper Prize of the 2015 Asia Pacific Microwave Conference, in 2015; the Merit Paper Prize of the 2016 International Symposium on InfoComm and Media Technology in Bio-Medical and Healthcare Application, Singapore, in 2016; and the Honorable Mention Award of the 2019 IEEE MTT-S International Wireless Symposium. She serves as a Reviewer for IEEE Access and IEEE Antennas and Wireless Propagation Letters.

KUO-SHENG CHIN (Senior Member, IEEE) received the B.S. degree in electrical engineering from the Chung Cheng Institute of Technology, Taoyuan, Taiwan, in 1986, the M.S.E.E. degree from Syracuse University, Syracuse, NY, USA, in 1993, and the Ph.D. degree in communication engineering from National Chiao Tung University, Hsinchu, Taiwan, in 2005. From 1986 to 2005, he was with the Chung Shan Institute of Science and Technology, Taoyuan, as a Research Assistant, becoming an Assistant Scientist, and then an Associate Scientist. In 2006, he joined Chang Gung University, Taoyuan, as a Faculty Member, where he is currently a Professor with the Department of Electronic Engineering. His current research interests include microwave and millimeter-wave couplers, filters, duplexers, low-temperature cofired ceramic circuits, automotive radar antennas, frequency-selective surfaces, filtering antennas, radomes, and electromagnetic pulse research. He was a recipient of the Outstanding Teacher Award from Chang Gung University, in 2014 and 2021. He was one of the recipients of the Best Paper Award of the International Conference on Electromagnetic Near Field Characterization and Imaging, in 2009; the Honorable Paper Award of the International High Speed Intelligent Communication Forum, in 2010; the Best Student Paper Award of the International Symposium on Next-Generation Electronics, in 2014; the Best Paper Award of Taiwan Precision Engineering Workshop, in 2016; and the Best Student Paper Award of 2018 The 8th International Symposium on InfoComm and Mechatronics Technology in Bio-Medical and Healthcare Application. He supervised a student team to win first place in the 2009 National Electromagnetism Application Innovation Competition, Taiwan. He served as an Associate Editor for *Microwave and Optical Technology Letters*, from 2019 to 2020.